

Synchronization dynamics on the EU and US power grids

Géza Ódor,^{1,*} Shengfeng Deng,^{1,†} Bálint Hartmann,² and Jeffrey Kelling^{3,4}

¹*Centre for Energy Research, Institute of Technical Physics
and Materials Science, P. O. Box 49, H-1525 Budapest, Hungary*

²*Centre for Energy Research, Institute for Energy Security
and Environmental Safety, P. O. Box 49, H-1525 Budapest, Hungary*

³*Faculty of Natural Sciences, Technische Universität Chemnitz,
Straße der Nationen 62, 09111 Chemnitz, Germany*

⁴*Department of Information Services and Computing,
Helmholtz-Zentrum Dresden-Rossendorf, P. O. Box 51 01 19, 01314 Dresden, Germany*

Dynamical simulation of the cascade failures on the EU and USA high-voltage power grids has been done via solving the second-order Kuramoto equation. We show that synchronization transition happens by increasing the global coupling parameter K with metastable states depending on the initial conditions so that hysteresis loops occur. We provide analytic results for the time dependence of frequency spread in the large K approximation and by comparing it with numerics of $d = 2, 3$ lattices, we find agreement in the case of ordered initial conditions. However, different power-law (PL) tails occur, when the fluctuations are strong. After thermalizing the systems we allow a single line cut failure and follow the subsequent overloads with respect to threshold values T . The PDFs $p(N_f)$ of the cascade failures exhibit PL tails near the synchronization transition point K_c . Near K_c the exponents of the PL-s for the US power grid vary with T as $1.4 \leq \tau \leq 2.1$, in agreement with the empirical blackout statistics, while on the EU power grid we find somewhat steeper PL-s characterized by $1.4 \leq \tau \leq 2.4$. Below K_c we find signatures of T -dependent PL-s, caused by frustrated synchronization, reminiscent of Griffiths effects. Here we also observe stability growth following the blackout cascades, similar to intentional islanding, but for $K > K_c$ this does not happen. For $T < T_c$, bumps appear in the PDFs with large mean values, known as “dragon king” blackout events. We also analyze the delaying/stabilizing effects of instantaneous feedback or increased dissipation and show how local synchronization behaves on geographic maps.

I. INTRODUCTION

With the power sector undergoing huge changes, the modelling of power grids has become a focus point for researchers in the fields of statistical physics as well. The hierarchical modular structure (or HMN) of these networks, their heterogeneity and their size make them a perfect candidate for complex system analysis, as discussed in [1–3]. The shift from traditional fuels to large scale utilization of renewable energy sources poses a number of challenges in regards of robustness and resilience of power systems, mainly due to the appearing correlated spatio-temporal fluctuations. Sudden changes (e.g. intermittent production, load ramps, outages) may start desynchronization cascades, which would propagate through the whole synchronously operated system as an avalanche. The resulting blackouts are of various sizes, but they often lead to full system desynchronizations lasting for extended periods [4]. The size distributions of the outages have been found scale-free in the US, China, Norway, Sweden in the available long time series data. In particular, power-laws could be fitted in countries, with so called robust networks [5], where the networks are categorized as robust or fragile based on static network topology analysis. As defined by [6], networks with

$P(k > K) = C \exp(-k/\gamma)$ cumulative degree (k) distribution and $\gamma < 3/2$ are called robust.

The research community is actively working on methods to support understanding and forecasting of such events [7]. More particularly, taking the aspect of statistical physics, risk of failure in power systems represents a specific case of the risk of system-wide breakdown in threshold activated disordered systems. Self-organized criticality (SOC) [8] is typically used for the modelling of such phenomena [9], where SOC is expected to arise as the consequence of self-tuning to a critical point, which is determined by the competition of power needs and transmission capabilities of the grid itself. DC threshold models [10] can be extended by considering AC power flows of power systems, modelling them via the second order Kuramoto equation [11]. An increasing number of papers discuss synchronization and stability issues by this approach, such as in Refs. [12–23].

These solutions can be deduced from the power transmission behavior of AC systems and are actually a generalization of the Kuramoto model [24] with inertia. Below $d < d_l = 4$ the Kuramoto model does not exhibit real phase transitions to a synchronized state, but a smooth crossover [25]. In real life, partially synchronized states can be observed. It was also observed that in lower graph dimensions the transition point shifts towards infinity as the system size and hysteresis behavior emerge [3].

Highly heterogeneous systems (often referred to as disordered with respect to the homogeneous ones) can exhibit rare region effects, which alter critical dynam-

*odor.geza@ek-cer.hu

†shengfeng.deng@ek-cer.hu

ics [26]. Such rare regions, locally in different state than the remainder of the network, evolve slowly and contribute to the global order parameter, causing slow dynamics and fluctuations. They can generate so-called Griffiths Phases (GP) [27] in an extended region around the critical point, causing slowly decaying auto-correlations and burstiness [28]. Their existence in load driven power-grid and earthquake models is studied very recently by [29]. These rare regions can also lead to frustrated synchronization and chimera states [30–32], which result in non-universal PL distributions of the desynchronization events below the transition point [3, 33–35]. The authors have previously provided evidence for this using the second order Kuramoto model on 2d lattices and large synthetic power system topologies [3] and on the realistic representation of the Hungarian power system while also allowing line outages (line-cuts) [36].

The second order Kuramoto model with power transmission thresholds (line capacities) has been also introduced in [36, 37] for the dynamical modelling of cascade events. Identification of critical lines of transmission in different national power grids has been determined. We follow this method in order to investigate the desynchronization duration distributions via measuring the number of failed lines following a link removal event. We shall also compare results obtained on 2d and 3d lattices with those of the US and EU high voltage power-grid. Multiple recent studies suggested that it is possible to prevent the spread of cascade failures either by adding an isolator as a fortress against an attack [38], or by adding some nodes to increase the rerouting path, or by strengthening a link [39]. Surprisingly, we observed that it is also possible to increase the synchronization level by triggering moderate cascade line failures for more weakly coupled power grids. This effect bears a close resemblance to the so-called “intentional islanding operation” in which the spread of failures could be contained by removing some weak links so that a power grid is segregated into several self-sustained islands [40, 41]. As coupled oscillators described by the second order Kuramoto model exhibit a discontinuous synchronization transition, cascade distributions are expected to consist of two different types of avalanches, regular ones and huge avalanches or kings [42], corresponding to the bumps in the distributions. Recently these kings, also called “Dragon Kings” (DK), were shown to exist in sand-pile models, following self-organized bistability [43], which is expected to be a common phenomenon in nature. Very recently, in a sand-pile model, coupled to massless Kuramoto oscillators, designed to model power-grids the existence of DK-s has also been shown [44]. We also show the appearance of DK-s in our power-grid simulations, based on the swing equations of the AC circuits.

The remainder of this paper is organized as follows: In Sec. II we describe the methods and the power grids to be used in the paper. In Sec. III, we first explore the temporal evolution of the frequency spread and the phase order parameter during thermalization and after invoking one

random line cut. We also give a qualitative explanation for the frequency spread algebraic decay via a linear approximation argument [45]. We then present numerical results for cascades for the EU-HV and US-HV networks. These results show that in the neighborhood of criticality, cascade sizes can display non-universal power laws and there is also a manifestation of islanding effects [40, 41]. In Sec. IV, we briefly demonstrate that the local Kuramoto order parameter is not uniform across different geographical regions. Finally, Sec. V summarizes this work.

II. MODELS AND METHODS

In the lack of full details of power-grids, as a first approximation, the evolution of synchronization is described by the swing equations [46] set up for mechanical elements with inertia by the second-order Kuramoto equation [11]. For a network of N oscillators with phase $\theta_i(t)$:

$$\begin{aligned}\dot{\theta}_i(t) &= \omega_i(t) \\ \dot{\omega}_i(t) &= \omega_i(0) - \alpha\dot{\theta}_i(t) + K \sum_{j=1}^N A_{ij} \sin[\theta_j(t) - \theta_i(t)] ,\end{aligned}\tag{1}$$

where α is the damping parameter, describing the power dissipation, or an instantaneous feedback [36], K is a global coupling, related to the maximum transmitted power between nodes and A_{ij} , which is the adjacency matrix of the network containing admittance elements. The self-frequency of the i -th oscillator $\omega_i(0)$ describes the power in/out of a given node when Eq. (1) is considered to be the swing equation of a coupled AC circuit.

In our simulations the following parameter settings were used: the α dissipation factor, which is chosen to be equal to 0.4 to meet expectations for power-grids, with the $[1/s]$ inverse time physical dimension assumption. For modeling instantaneous feedback, or increased damping parameter we applied: $\alpha = 3.0[1/s]$ similarly as in [36].

To solve the differential equations we used the adaptive Bulirsch-Stoer stepper [47] in general, which provides more precise results for large K coupling values. To obtain reasonable statistics, via the adaptive solver we needed very strong computing resources, using parallel codes running on GPU clusters by utilizing the VexCL library for vector operations [48], but the results were cross-checked with the results obtained on conventional CPU machines and compared with the Runge-Kutta-4 solvers too. The details of the GPU implementation will be discussed in a separate publication.

Exploiting the Galilean invariance of Eq. (1) we can gauge out the mean value $\langle\omega_i(0)\rangle$ in a rotating frame, thus for the self-frequencies $\omega_i(0)$ we used Gaussian random variables with zero mean and unit variance.

What is more, another rescaling invariance can also be discovered, similarly as in the case of the first-order

Kuramoto model [34]:

$$K' = aK, \quad \omega'_i(0) = a\omega_i(0), \quad \alpha' = \sqrt{a}\alpha, \quad t' = t/\sqrt{a}, \quad (2)$$

which could also be exploited by the solutions at very large couplings, where the adaptive solver may slow down substantially. Conversely, if the relaxation time (for smaller K) is too slow we could avoid it by increasing K . However, there is an optimal value for rescaling due to the balance between the speed gain for the solver by using a smaller K and the dilation of time by a factor of \sqrt{a} . This may be determined by actual simulations for a given network or parameter set. We measured that by choosing $a = 1/9$, with which, although the simulation time t' is increased by a factor of 3, the GPU run times became faster by a factor of 20% as compared to the runs without rescaling in case of large 2d lattices with linear sizes $L = 3000$. Further benchmark results will be published in a separate publication [49].

To achieve thermalized states with larger synchronization the initial state was set to be fully synchronized, with phases: $\theta_i(0) = 0$, but to determine the hysteresis curve or to investigate $\Omega(t)$ decays we also used the uniform random distribution: $\theta_i(0) \in (0, 2\pi)$. The initial frequencies were set as $\dot{\theta}_i(0) = \omega_i(0)$. The thermalization was performed by running the code for $1000 - 5 \times 10^4$ time steps, judging by visual or automatic inspection of the status of order parameter saturation, without allowing line cuts on the graph. This, is the so called "quench" procedure in statistical physics, which does not happen in reality, because in case of a cold restart both the consumers and generators are connected gradually and adiabatically, following a prescribed protocol to avoid initial unbalances. However, instead of the more tedious equilibration process we quenched the system from random or ordered initial conditions to a steady states without allowing cascade failures. This also has the advantage that we could learn the dynamics of the second-order Kuramoto model on different networks.

Following the thermalization we perturbed the system by removing a randomly selected link, or alternatively, a randomly selected node, in order to simulate a power failure event. Following that, if the ensuing power flow on a line between neighboring nodes was greater than a threshold:

$$F_{ij} = |\sin(\theta_j - \theta_i)| > T, \quad (3)$$

so that that line is regarded as overloaded, we removed this link from the graph permanently and measured the total number of line failures N_f of the simulated blackout cascades of each realizations, corresponding to different $\omega_i(0)$ self frequency values. At the end we applied histogramming to determine the PDFs of N_f . In the vicinity of criticality, one usually expects power-law distributions of the form

$$p(N_f) \sim N_f^{-\tau}, \quad (4)$$

thus we plotted our results on the log-log scale.

During the cascade simulations, which had the length of $t_{max} = 10^3 - 10^4$ we measured the Kuramoto phase order parameter:

$$z(t_k) = r(t_k) \exp[i\theta(t_k)] = \frac{1}{N} \left| \sum_j \exp[i\theta_j(t_k)] \right|, \quad (5)$$

by increasing the sampling time steps exponentially :

$$t_k = t_0 \times 1.08^k. \quad (6)$$

In Eq. (5), $0 \leq r(t_k) \leq 1$ gauges the overall coherence and $\theta(t_k)$ is the average phase. The set of equations (1) were solved numerically for $10^3 - 3 \times 10^4$ independent initial conditions, initialized by different $\omega_i(0)$ -s, and different $\theta_i(0)$ -s if applicable, and sample averages for the phase order parameter

$$R(t_k) = \langle r(t_k) \rangle \quad (7)$$

and for the variance of the frequencies

$$\Omega(t, N) = \left\langle \frac{1}{N} \sum_{j=1}^N (\bar{\omega} - \omega_j)^2 \right\rangle \quad (8)$$

were determined. In case of a single peaked self-frequency distribution, $\Omega(t, N)$ is an appropriate order parameter and is easier to measure, besides the more commonly used measure [45], which counts the number of oscillators in the largest cluster having an identical frequency.

In the steady state after thermalization we also measured the standard deviation of the order parameters $R(t_k)$ and $\Omega(t, N)$ in order to locate the transition point K_c by the fluctuation maxima. In case of the first-order Kuramoto equation the fluctuations of both order parameters show a maximum at the same K_c [35], meaning a maximal chaoticity here. For the second-order Kuramoto equation only $\sigma(R(t_k))$ seems to have a peak at K_c ; see Sec. III C and Sec. III D for more details. Nonetheless, one would expect chaotic dynamics to emerge in the vicinity of the transition point.

A. Description and analysis of the power grids

Here we determined some basic topological characteristics [50] of the studied power grids using the Gephi tool [51] and MATHEMATICA. For comparison, we have studied the dynamical behavior of the western US-HV power grid, obtained from [52], and of the EU-HV power grid, obtained from the "SciGRID Dataset" [53]. These power-grid networks are genuinely hierarchical modular networks if the detailed information for the medium- and low-voltage parts of the grids are also incorporated. Practically, it is almost impossible to infer the entire structure of a large power-grid network, but it is feasible to mimic a realistic power grid network by adding to the HV skeleton of the grid the medium- and low-voltage parts

TABLE I: Graph measures of the investigated power-grids.

	N	E	$\langle k \rangle$	γ	Q	L	L_r	C	σ	d
US	4194	6594	2.67	1.24(1)	0.929	18.7	17.7	0.08	9.334	3.0(1)
EU	13478	33844	2.51	1.53(5)	0.963	49.505	10.2	0.089	98.63	2.6(1)

according to the empirical hierarchical distribution, as we previously did in Ref. [3] for the Hungarian power-grid network. In this work, we will only focus on the high voltage networks as obtained from the raw data. For simplicity, all transmission lines are regarded as bidirectional and identical. Nodes are also identical and featureless.

Standard graph measures for the US-HV and the EU-HV networks are summarized in Table I. The US-HV network statistics were also summarized in [36]. The US-HV network consists of $N = 4194$ nodes and $E = 6594$ edges, while $N = 13478$ nodes of the EU-HV network are interconnected via $E = 33844$ links. The average degrees $\langle k \rangle$ of the two networks take very similar values 2.67 and 2.51, respectively. As an example, in Fig. 1, we show the degree distribution of the EU-HV network. The tail of the degree distribution ($k > 5$) may be fitted with a PL with a large exponent $\simeq 5$. However, it is more reasonable to fit the data by an exponential function, which is common for power grids [54, 55]. For $k \geq 15$ a stretched exponential $8.25 \times e^{-0.53(5)k}$ fits the data quite well. Furthermore, comparing the exponents γ of the cumulative degree distribution of the two networks renders EU-HV network to be just at the threshold of robust/fragile: $\gamma = 3/2$, according to the definition by [6], while the US-HV network can be categorized as a robust network.

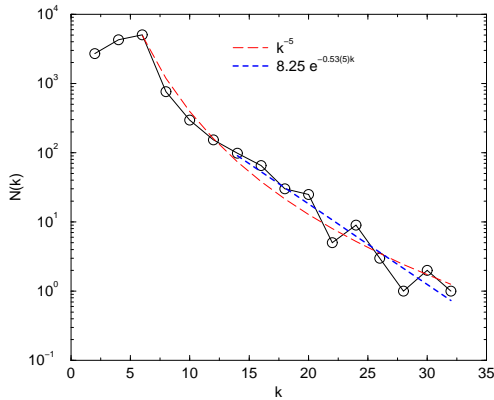


FIG. 1: Degree distribution of the EU-HV network. The blue dashed line shows an exponential fit for $k \geq 15$, while the red long-dashed line is a PL fit for $k > 5$.

The adjacency matrix of the EU-HV network is shown in Fig. 2. Similar to the US-HV network, this is a highly modular network with modularity quotient $Q = 0.964$, defined by

$$Q = \frac{1}{N \langle k \rangle} \sum_{ij} \left(A_{ij} - \frac{k_i k_j}{N \langle k \rangle} \right) \delta(k_i, k_j), \quad (9)$$

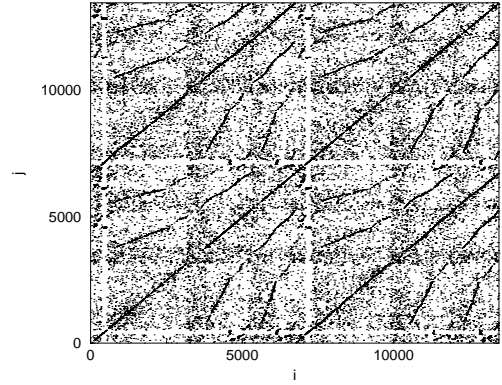


FIG. 2: The adjacency matrix of the EU-HV grid, with $A_{ij} = 1$ displayed in black and white if otherwise (c.f. [36] for the US-HV grid data).

where $\delta(i, j)$ is the Kronecker delta function.

The Watts-Strogatz clustering coefficient [56] of a network of N nodes is

$$C = \frac{1}{N} \sum_i 2n_i / k_i (k_i - 1), \quad (10)$$

where n_i denotes the number of directed edges, interconnecting the k_i nearest neighbors of node i . With $C_{US} = 0.08$ and $C_{EU} = 0.089$, both networks show a much higher clustering coefficient than that of a random graph with the same N and E , defined by $C_r = \langle k \rangle / N$. The $C_{EU} = 0.089$ is about 480 times higher, than that of a random network of same size $C_r = 0.000186229$.

The average shortest path length is

$$L = \frac{1}{N(N-1)} \sum_{j \neq i} d(i, j), \quad (11)$$

where $d(i, j)$ is the graph distance between vertices i and j . For a random graph of the same size and edge number, Ref. [57] gives the expression

$$L_r = \frac{\ln N - 0.5772}{\ln \langle k \rangle} + 1/2. \quad (12)$$

As shown in Table I, in case of the EU-HV network, L is much larger than L_r , in stark contrast to the US-HV network. Furthermore, according to the definition of the coefficient [58]:

$$\sigma = \frac{C/C_r}{L/L_r}, \quad (13)$$

the EU-HV network is a small-world network because $\sigma \simeq 100$, is much larger than unity.

To summarize, from Table I we can see that the EU-HV network has about 3 times more nodes and 5 times more edges than the western US-HV grid and exhibits similar measures, except for L , which is also ~ 2.5 times bigger. Furthermore, by the degree exponent it is marginally

fragile, unlike the US-HV grid which is robust, thus the existence of PL blackout size distributions is a matter of question. We shall investigate if this holds in the dynamical sense, in the presence of fluctuating energy resources.

In addition, we also provide estimates for the effective graph (topological) dimension d , defined by

$$N(r) \sim r^d, \quad (14)$$

where we counted the number of nodes $N(r)$ with chemical distance r or less from randomly selected seeds and calculated averages over many trials. In Fig. 3, we illustrate the growth of $N(r)$ for the EU-HV network. Note, however that finite-size cutoff happens already for $r > 30$. To see the corrections to scaling we determined the effective exponents of d as the discretized, logarithmic derivative of (14)

$$d_{\text{eff}}(r + 1/2) = \frac{\ln\langle N(r) \rangle - \ln\langle N(r+1) \rangle}{\ln(r) - \ln(r+1)}. \quad (15)$$

These local slopes are shown in the inset of Fig. 3, as the function of $1/r$ and enables an extrapolation to $1/r \rightarrow 0$. This gives a smaller value $d = 2.6(1)$ for the EU-HV network, than in case of the US-HV network $d = 3.0(1)$.

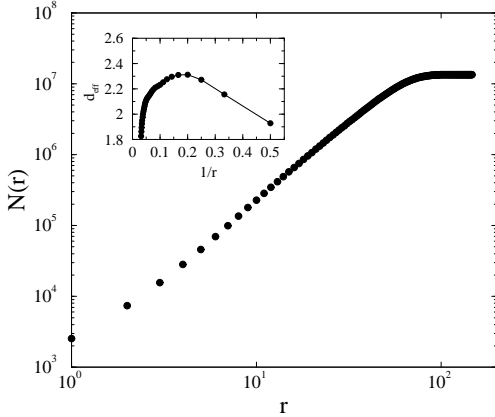


FIG. 3: Number of nodes with distance r or less from random seeds in the breadth-first search algorithm applied for the EU-HV graph. The inset shows the local slopes, corresponding to the same data. Linear extrapolation to $1/r \rightarrow 0$ provides $d = 2.6(1)$.

III. SYNCHRONIZATION DYNAMICS ON THE POWER GRIDS

A. Frequency entrainment for large K

It is known that on a d -dimensional lattice, the frequency order parameter (8) decays as $\Omega \propto t^{-d/2}$ in case of the first-order Kuramoto model in the large coupling limit [45]. Following Ref. [45], we have investigated this in the case of the second-order Kuramoto model, first by

applying a linear approximation by replacing $\sin(x) \propto x$ to gain a qualitative understanding. In a d -dimensional space, casting the continuum second-order Kuramoto equations into the momentum space, we are led to solve

$$\frac{\partial^2}{\partial t^2} \theta(\mathbf{k}, t) + \alpha \frac{\partial}{\partial t} \theta(\mathbf{k}, t) = \omega(\mathbf{k}, 0) - K k^2 \theta(\mathbf{k}, t). \quad (16)$$

Without citing the cumbersome solution, we simply give the expression for the phase velocity $[\omega(\mathbf{x}, t) \equiv \dot{\theta}(\mathbf{x}, t)]$ in the Fourier space

$$\omega(\mathbf{k}, t) = e^{-\frac{1}{2}t(\alpha+\Delta)} \left[\omega(\mathbf{k}, 0) ((\Delta + 2 - \alpha)e^{\Delta t} + \alpha + \Delta - 2) - 2K k^2 \theta(\mathbf{k}, 0) (e^{\Delta t} - 1) \right] / 2\Delta, \quad (17)$$

where $\Delta = \sqrt{\alpha^2 - 4Kk^2}$. In the initial short-time regime, $\omega(\mathbf{k}, t)$ displays a transient oscillation (also cf. Fig. 4) for modes $k > \alpha/2\sqrt{K}$, but they are quickly suppressed by the factor $e^{-\frac{1}{2}t}$. Similar to the first-order Kuramoto model [45], all Fourier modes of $\omega(\mathbf{k}, t)$ and now *including* the $\mathbf{k} = 0$ mode also vanish in the long-time limit, suggesting that the phase velocity becomes uniform and the frequency spread Ω approaches zero. This is immediately verified by the explicit expression for Ω :

$$\begin{aligned} \Omega(t) &= \frac{1}{L^d} \int d^d \mathbf{x} \langle [\omega(\mathbf{x}, t) - \bar{\omega}(t)]^2 \rangle \\ &= C_d \int_{2\pi/L}^{\pi/a} dk k^{d-1} \frac{e^{-t(\alpha+\Delta)}}{4\Delta^2} \left[\alpha + \Delta - 2 \right. \\ &\quad \left. + (\Delta - \alpha + 2)e^{\Delta t} \right]^2, \end{aligned} \quad (18)$$

where $\bar{\omega}(t)$ denotes the spatial average of $\omega(\mathbf{x}, t)$, while a and C_d are the lattice spacing and the geometric factor, respectively, both of which can be innocuously taken as 1 for a qualitative analysis.

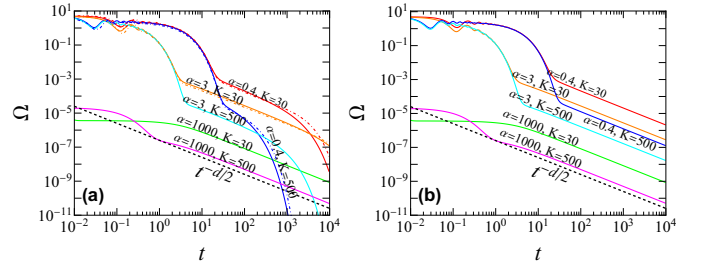


FIG. 4: The frequency spread for $d = 2$, obtained through numerical integration of Eq. (18) at different α and K values for (a) $L = 3000$ and (b) $L = 10^{12}$. For comparison, the dot dashed lines show the full results of Eq. (1) with synchronized initial conditions and the dashed lines mark the algebraic decay law $t^{-d/2}$ of the first-order Kuramoto model.

As shown in Fig. 4 (b), for a large enough system, after a short initial oscillatory transition, the frequency

spread display the same algebraic decay (in the intermediate short-time regime $1 \ll t \ll L/\sqrt{K}$) as that of the first-order Kuramoto model, as long as $\alpha > 0$ and $K > 0$. This is most evident for the scenario when $\alpha \gg 1$ as the damping term becomes essentially dominant over the second-order term. In smaller systems, due to finite-size effects, the algebraic decay may give way to a more rapid decay for smaller α and larger K values [cf. Fig. 4(a)], with which, one may still observe a distorted algebraic decay in the intermediate time range.

It should be emphasized that linear approximation inevitably missed out nonlinearity of the system as well as the effects of heterogeneity in the initial frequency/phase distribution and in the topological structure. Hence, an intermediate algebraic decay may also be observed for the frequency spread by explicitly solving Eq. (1), but it doesn't necessarily follow $t^{-d/2}$, e.g. due to nonlinearity. In particular, most realistic complex networks are characterized by a relatively small average shortest path length (see e.g. Table I) as well as a more heterogeneous structure, the latter of which could even render linear approximation invalid. Both these two factors may then strongly suppress any manifestation of an elongated algebraic decay for networks, except for a certain critical coupling value, which is exactly what we observed for the EU-HV and the US-HV networks, as will be shown in below with respect to the US-HV network.

To this end, we solved Eq. (1) on $L = 3000$ (2d) and $L = 260$ (3d) linear sized lattices, with periodic boundary conditions, as well as on the EU-HV and the US-HV networks. Averaging was done over 100 – 1000 samples of different initial self frequencies. Although the linear approximation shows good agreement with simulation results, when we start from a fully synchronized state, as Figs. 5 and 6 show, the $\Omega(t)$ spread decays exhibit non-trivial K - and α -dependent PL-s for large global couplings if a disordered initial state $[\theta_i(0) \in (0, 2\pi)]$ is implemented. The fitted decay exponents τ change in the range $1.2 \leq \tau \leq 1.5$ in the 2d case. Solutions on the 3d lattice provide PL tails, with exponents $\tau \simeq 1.85$. Therefore, the decay exponents are slightly larger than $d/2$, due to the non-negligible phase fluctuations.

In contrast to lattices, in the case of the US-HV network on which the linear approximation fails, algebraic decay is only observed at $K_c = 20$ with a larger $\alpha = 3$. The PL tails, before size cutoff, seem to agree with the regular lattice results, the fitted exponent is around $\tau \simeq 1.5 \approx d/2$. Note that the effective graph dimension of the US-HV network is between 2 and 3, but an extrapolation to $N \rightarrow \infty$ gives $d = 3.0(1)$ shown in Table I.

B. The effects of line cut and instantaneous feedback

In this section, we introduce a random transmission line cut to thermalized, stable systems. As shown in Figs. 7 and 8, after the systems transited into their sta-

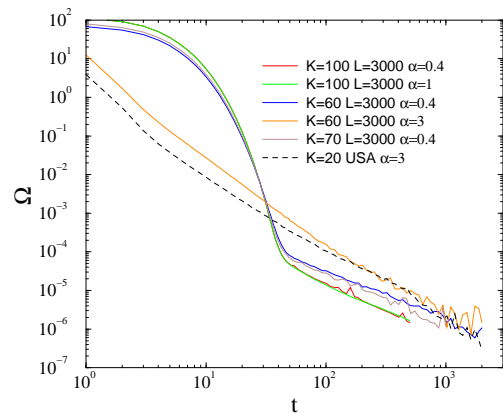


FIG. 5: Evolution of frequency spread order parameter on the 2d lattices as the function of K and α values shown by the legends in case of disordered initial conditions. These curves exhibit PL tails within the exponent range $1.2 \leq \tau \leq 1.5$. For comparison the dashed line shows the result for the US-HV network at $K = 20$ and $\alpha = 3$, for which $\tau \simeq 1.5$ can be read off.

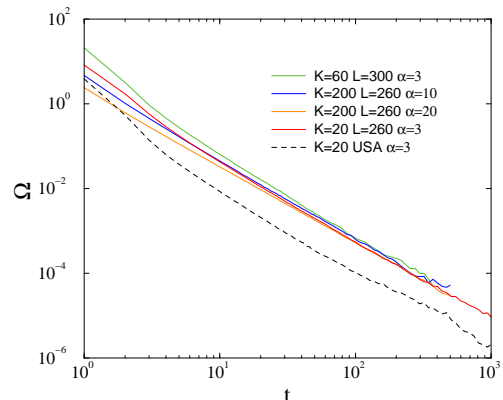


FIG. 6: Evolution of frequency spread order parameter on the 3d lattices as the function of K and α as shown by the legends in case of disordered initial conditions. These curves exhibit PL tails, with similar exponents $\tau \simeq 1.85$. For comparison the dashed line shows the result for the US-HV at $K = 20$ and $\alpha = 3$, where $\tau \simeq 1.5$ can be read off.

tionary states with a thermalization process without allowing any line failures, a subsequent random line cut introduces a perturbation, that can trigger a cascade of line failures dictated by the overload condition (3) and hence decrease the synchronization level. In accord with our intuition, systems with a lower threshold value (i.e. lines are more vulnerable against disturbances) usually are affected to a greater extent by one line cut, transiting into a new stationary state with a lower phase order parameter value and a broader frequency spread. However, this may not always be the case. As can be seen in the case of the EU network, the phase order parameter may even increase after one line cut for certain intermediate threshold values (e.g. $T = 0.2$), irrespective of the fact

that the frequency spreads are actually increased. This hints that it is also possible to make certain power grid more stable by removing some of its links, as long as lines are not removed too destructively with respect to a very low threshold. Such power grids may provide a prototype for studying the factors that affect the stability of power grids. Especially, this effect is in analogous to the “islanding effect” [40, 41]. We will revisit its implication further in the subsequent subsections.

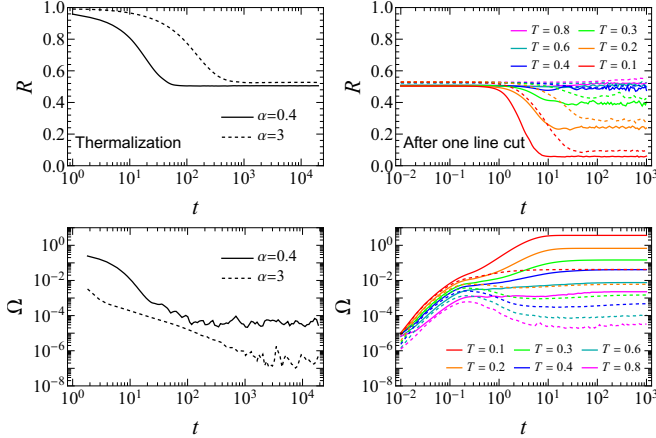


FIG. 7: Evolution of phase order parameter (top) and frequency spread order parameter (bottom) of the US network at $K = 20$ during thermalization (left) and after one subsequent line cut (right) with respect to different thresholds (right: $T = 0.1, 0.2, \dots, 0.8$). Comparing to the normal case $\alpha = 0.4$ (solid lines), a negative feedback $\alpha = 3$ (dashed lines) essentially slows down the dynamics of the phase order parameter, while at the same time leads to a smaller frequency spread; similar effects are observed following one line cut.

Furthermore, we note that, acting as a damping force, a negative instantaneous feedback $\alpha = 3$ plays the role of slowing down the dynamics of the phase order parameter and at the same time suppressing the eventual frequency spread. A slightly smaller level of decrease in $R(t)$ also happens. For certain threshold value, such as the case for $T = 0.6$ in Fig. 8, a negative feedback caused nontrivial effect, where the frequency spread is dropped by several orders of magnitude. Therefore, mechanisms for negative feedback would be desirable in designing power grids if achieving a high frequency entrainment is crucial.

Now that we have learned the overall picture for the evolution processes during thermalization and after carrying out one line cut, in the next two subsections, we quantify the changes induced by one line cut for the US-HV network and EU-HV network, separately.

C. US-HV power-grid results

We have repeated the analysis performed in [3] for the US-HV network with the difference that now we do not allow line cuts in the thermalization, as discussed in the previous subsection. This is a more realistic approach,

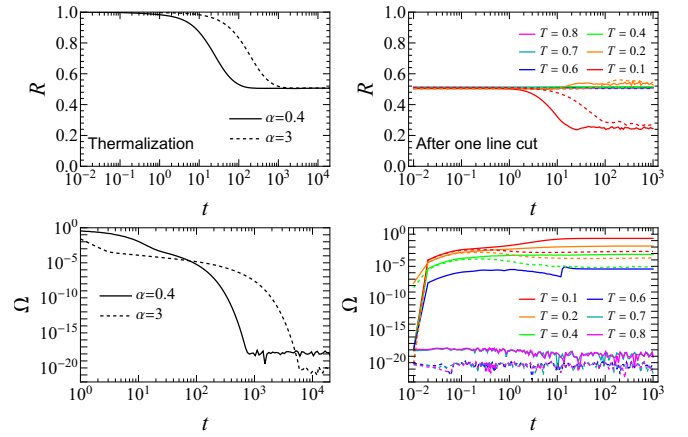


FIG. 8: Evolution of phase order parameter (top) and frequency spread order parameter (bottom) of the EU network at $K = 80$ during thermalization (left) and after one subsequent line cut (right) with respect to different thresholds (right: $T = 0.1, 0.2, 0.4, 0.6, 0.8$). Comparing to the normal case $\alpha = 0.4$ (solid lines), a negative feedback $\alpha = 3$ (dashed lines) essentially slows down the dynamics of the phase order parameter, while at the same time leads to a smaller frequency spread; similar effects are observed following one line cut.

as we avoid failures in the grid by a sudden restart. In reality such restart happens by a slow, adiabatic procedure, gradually switching on generators and consumers by a prescribed power system protocol.

Generally we started the thermalization processes from fully synchronized state: $\theta_i(0) = 0$ in order to arrive at higher steady states than in case of quenching from random initial conditions. This difference comes from the hysteretic behavior of the second-order Kuramoto solution. As Fig. 9 shows the $R(t \rightarrow \infty)$ fluctuations, measured in the steady state of this thermalization at $t = 20000$ exhibit peaks as before, published in [3], but they occur at a smaller value. We can estimate them as $K_c \simeq 22(2)$ for $\alpha = 0.4$ and $\alpha = 3$ both.

The synchronization transition behavior can also be seen in the $\Omega(t)$ decays, starting from disordered states for $\alpha = 3$, US-HV, as shown by the inset of Fig. 9. For $K > K'_c$ the decay is exponentially fast, for $K < K'_c$ the curves saturate to finite Ω values, while at $K'_c = 20$ a PL decay occurs, characterized by the exponent $\tau \simeq 1.5$, as one can read off from the inset of Fig. 9. It is interesting to see that $K'_c \approx K_c$ on the US-HV network, but we should see later that is not always the case.

In [3] $K_c \simeq 60(10)$ was published in case of $\alpha = 3$, which is reasonable, since in the thermalization process line cuts were allowed, thus higher coupling was needed to stabilize the synchronization. Note that in the case of the frequency spread order parameter we don't find a peak in $\sigma(\Omega(t \rightarrow \infty))$, unlike for the first-order Kuramoto solutions [35], thus Ω does not become more chaotic at the transition.

Yet another advantage of the above-prescribed thermalization process is that one can initiate failure cascades

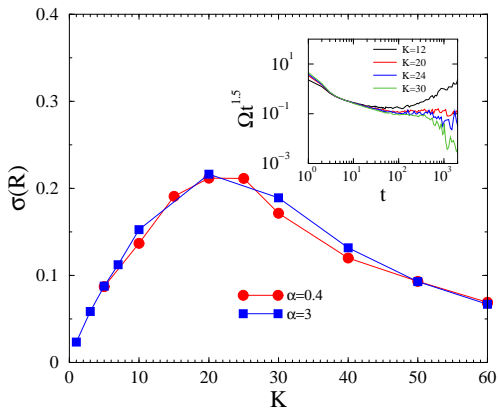


FIG. 9: Fluctuations of $R(t \rightarrow \infty)$ in case of the US-HV power grid at the end of the thermalization process. Both for the normal $\alpha = 0.4$ and the $\alpha = 3$ dissipation cases. Partial synchronization transition occurs at $K_c \simeq 22(2)$. The inset shows the decay of $\Omega(t)$ starting from disordered states at $\alpha = 3$ and for different global couplings, as shown by the legends. The curves are multiplied by a factor $t^{1.5}$ in order to see the scaling at $K_c = 20$.

by a single line or node removal, unlike by the procedures followed in [36]. This alters the steady state values and the synchronization transition peaks as compared the results published in [36].

In the previous subsection, we observed that for some intermediate T values the order parameter R may even increase following one line cut, despite the fact that cascade line failures may follow. To scrutinize this intriguing observation more closely, the relative change of the steady state $R(T)/R(T=1)$ values, following the cascade, are shown in Fig. 10. Islanding effects occur if K is lower than the thermalization value $K_c \simeq 20$ for $T \gtrsim 0.5$, which is maximal at $T_c \simeq 0.7$ (see the inset of Fig. 10). One may understand this by noting that, on the one hand, cascade line failures could bring about disturbances and render the system desynchronized, and on the other hand, however, with quite a proportion of the lines being removed, the network gradually becomes less and less connected and eventually prevent failures from being spread further, allowing an even higher synchronization level similar to the “islanding effect” [40, 41]. The observed islanding effect is thus a consequence of the delicate competition of these two factors, so that this effect is peaked at T_c , where the increased fluctuations most efficiently do the job (cf. Fig. 16 for a stronger justification). However, by tuning a system into a very vulnerable state with a very small T value, the system becomes quite unstable and failures will always prevail. The system is then tremendously desynchronized. In the inset of Fig. 10 we also show the $\sigma(R(T, K))$ values for different K and T control parameters. One can observe a smooth transition for the peaks, suggesting $T_c \rightarrow 0$ as we increase K .

The US-HV cascade size distributions $p(N_f)$ published in [36] remain the same for $K = 30$, as demonstrated on

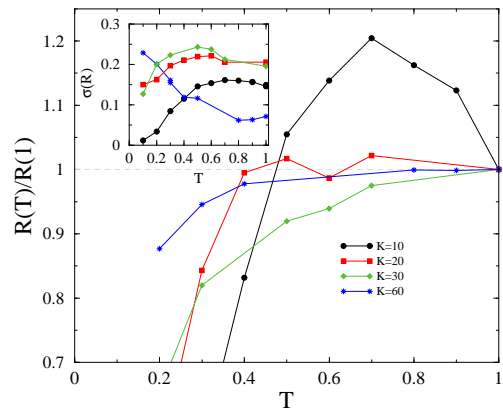


FIG. 10: Relative change of the steady state Kuramoto order parameter at $\alpha = 0.4$ as the consequence of the cascade in the US-HV power grid. The $R(T=1)$ values are set to be the reference points and $R(T)/R(T=1)$ is plotted. The gray dashed line marks the baseline for the emergence of islanding effects. The inset shows $\sigma(R(T, K))$.

Fig. 11. The estimated exponent values are also in good agreement with empirical estimations [10]. For $K = 20$ we could find $p(N_f)$ with PL tails, at $T \geq 0.9$ only. Here we could fit for the narrow region $N_f < 10$ a PL with an exponent $\tau = 1.6(3)$, as shown in Fig. 12. As we increase T from 0.5, we can see slowly decaying $p(N_f)$ curves, with an exponential cutoff for $N_f > 20$. For $T < 0.5$ thresholds, bumps in the PDFs with large mean values appear, suggesting Dragon King (DK) events of cascade failures. However, these DK bumps do not appear for couplings $K > K_c$.

Note, the forms of $p(N_f)$ do not change as we increase the dissipation/feedback factor from $\alpha = 0.4$ to $\alpha = 3$. The PDFs are also insensitive for the mode of initial perturbation, i.e. whether an edge or a node removal is committed after the thermalization. This kind of invariance was also found in [36] where even multiple perturbations caused the same kind of cascade size distribution forms.

D. EU-HV power-grid results

By determining the steady state values of R after the thermalization we can investigate the type of transition as it was done for the US-HV case. The adaptive solver allowed us to provide precise values even for very large K values. Similar to the US-HV grid we again found a smooth crossover from desynchronization to partial synchronization (which is merely indicated by the $\sigma(R)$ peaks for the US-HV case in Fig. 9) by increasing the global coupling K , as shown on Fig. 13. We can observe a hysteresis, where the upper branch corresponds to a start from an ordered, while the lower branch to a disordered initial state. The upper branch is insensitive to α , but for very large K -s the Runge-Kutta-4 algorithm breaks down and provides nonphysical, decreasing order param-

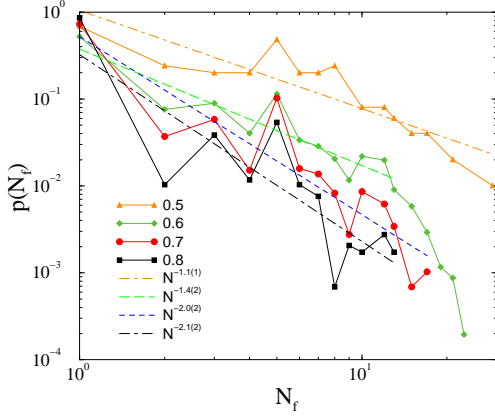


FIG. 11: Probability distribution of line failures for $K = 30$, $\alpha = 0.4$ and different thresholds marked by the legends in case of the US-HV power grid. Dashed lines show power-law fit for the scaling region, determined by visual inspection.

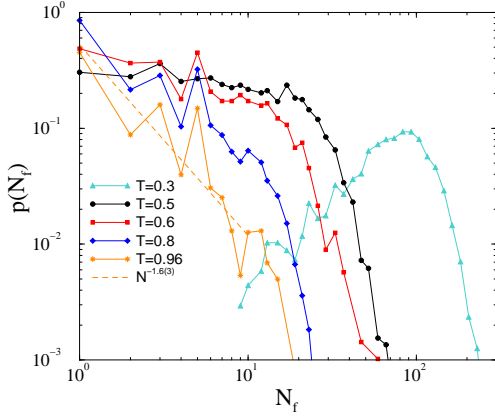


FIG. 12: Probability distribution of line failures for $K = 20$, $\alpha = 0.4$ and different thresholds marked by the legends in case of the US-HV power grid. DK cascade failures at $T = 0.3$ can be observed.

eter values. We have also measured the fluctuations of R over many samples. The inset of Fig. 13 shows that for the upper branch a peak occurs at $K \simeq 100$ marking a transition there. For random initial states the fluctuation peaks seem to occur at much higher couplings, that we could not investigate in detail as the adaptive solver slows down substantially for large K values.

We have also investigated the cascade size distributions for $\alpha = 0.4, 3$, $K = 20, 60$, and 80 , i.e. near the synchronization transition point $K_c \simeq 100$. For the low $K = 20$ we could only find log-normal like PDFs, with increasing mean values as T is decreased; see Fig. 18 in the Appendix, in which we also demonstrate the invariance of $p(N_f)$ with respect to an initial line or node removal. Still below the synchronization transition point K_c , at $K = 60$ one finds very few cascade line failures for $T > 0.5$, PDFs with continuously changing PL tails for $0.5 \leq T \leq 0.4$ and log-normal like distributions for

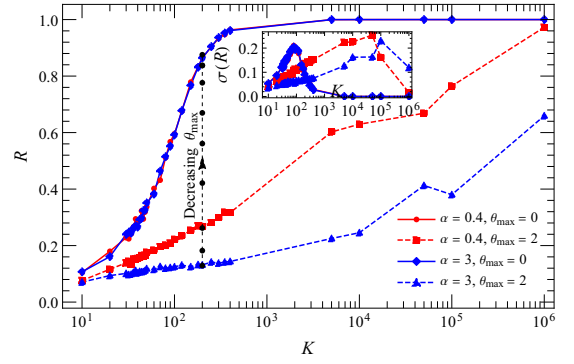


FIG. 13: The steady state values of the Kuramoto order parameter for the EU-HV network. Start from ordered/disordered initial states causes a hysteresis loop, closing at $K \sim 10^6$ for $\alpha = 0.4$. For $\alpha = 3$ we could not reach the closure point as for this large value the adaptive solver becomes very slow. There exists infinite intermediate branches if we initialize the phases as $\theta_i(0) \in (0, \theta_{\max})$ with different θ_{\max} values. The inset shows $\sigma(R)$, in which the peaks of the solid curves indicate $K_c \simeq 100$.

$T < 0.5$ (see Fig. 14). The small threshold distributions resemble to the so called “Dragon King” events described in Refs. [42, 44], while in the $0.5 \leq T \leq 0.4$ region, the continuously changing exponents $1.4 \leq \tau \leq 2.4$ suggest Griffiths effects as the consequence of the heterogeneity. Note, that Griffiths effects may also occur near mixed order transitions, where the steady state values jump, but dynamical scaling persists [59].

Near the transition point, at $K = 80$ the situation is different as shown on Fig. 15. Here PL tails emerge in the region $0.33 \leq T \leq 0.46$, which could be fitted by the exponents $1.3 \leq \tau < 3.0$, but part of these exponent values are larger than the empirical data and simulations of Refs. [9, 10], $1.3 \leq \tau \leq 2$ obtained for many countries. As these PL decays are very steep and occur for $N_f < 20$ only, it is hard to differentiate them from the tail of a Gaussian distribution. For $T < 0.22$ thresholds we can find the emergence of bumps, suggesting DK events.

As thermal noise may occur in real systems, which has not been considered up to now, but fluctuations, which came from the nonlinear chaoticity, we have also investigated the effect of an additional Gaussian noise. Without showing the preliminary results, we remark that the zero centered annealed noise, with unit variance did not modify the shape of the PDF, but shifted the noiseless $T = 0.33$ result to $T = 0.56$. Further analysis of the thermal noise is in progress, using the Euler-Maruyama adaptive solver, that can avoid the problem with Bulirsch-Stoer and the inaccuracies of Runge-Kutta-4 at large couplings.

We have compared the stability of steady states of the US-HV and EU-HV systems as the consequence of the failure cascades by measuring $R(t \rightarrow \infty)$. Since the sizes and dimensions of the networks differ, we determined the relative change of R (Fig. 16) as in the case of US-HV

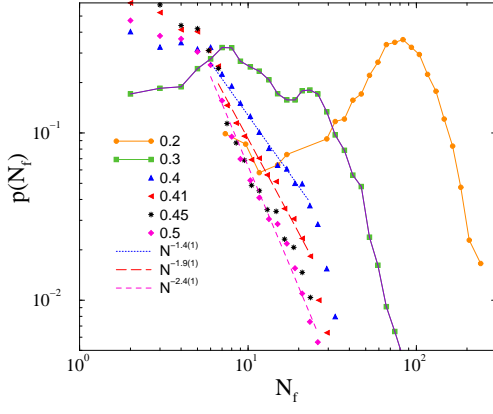


FIG. 14: Probability distribution of line failures for different thresholds for $K = 60$ shown in the legends in case of the EU-HV power grid. Dashed lines show power-law fits for the scaling region, determined by visual inspection. One can observe DK bumps for low thresholds.

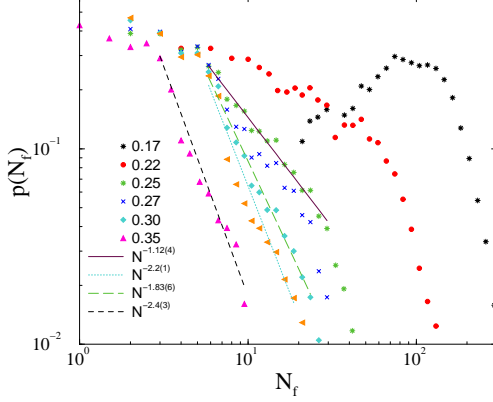


FIG. 15: Probability distribution of line failures for different thresholds for $K = 80$ shown in the legends in case of the EU-HV power grid. Dashed lines show power-law fits for the scaling region determined by visual inspection. One can observe DK bumps for low thresholds.

network. Again, we can see the “islanding” stabilization effect on the networks after the cascade failures, known in the power-grid engineering literature [40, 41]. As mentioned in the last subsection, this happens near $T_c(K)$, as one can read off from the inset of Fig 16, but gradually disappears for large K above K_c .

Note, that the maxima of these curves also agree with the T values by which the $p(N_f)$ decays exhibit power-law decay behavior. Hence, the system displays some nontrivial critical dynamics in the vicinity of criticality (K_c, T_c). We can also see that the increase of the dissipation factor from $\alpha = 0.4$ to $\alpha = 0.3$ does not change a lot, but enhances the islanding effect; compare the $K = 60$ curves in Fig. 16.

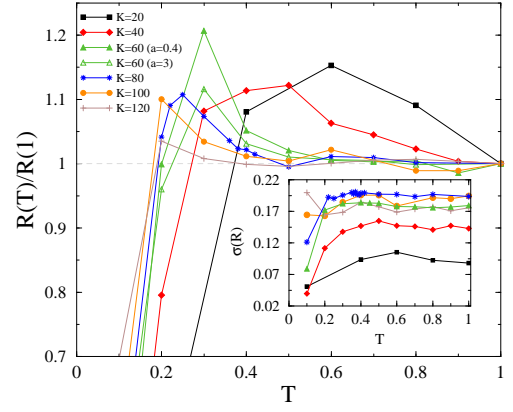


FIG. 16: Relative change of the steady state Kuramoto order parameter at $\alpha = 0.4$ the consequence of the cascade in the EU-HV grid. The $R(T = 1)$ values are set to be the reference points and $R(T)/R(T = 1)$ is plotted. The gray dashed line marks the baseline for the emergence of islanding effects. The inset shows $\sigma(R(T, K))$.

IV. LOCAL KURAMOTO RESULTS

To investigate the heterogeneity further we also measured the local Kuramoto order parameter, defined as the partial sum of phases for the neighbors of node i

$$r_i(t) = \frac{1}{N_{i,\text{neigh}}} \left| \sum_j^{N_{i,\text{neigh}}} A_{ij} e^{i\theta_j(t)} \right|, \quad (19)$$

and the power-flows F_{ij} defined in Eq. (3). This local Kuramoto measure was firstly suggested by Restrepo *et al.* [60, 61] to quantify the local synchronization of nodes, which allows us to follow the synchronization process by mapping the solutions on the geographical map. One example for the EU-HV grid is shown in Fig. 17, which is the result of thermalization after averaging over 1000 samples, initiated by random self-frequencies at $K = 80$ and $\alpha = 0.4$, rendering the grid close to the transition point. The map reveals strongly synchronized (green) regions as well as some weakly synchronized ones, especially near sea cable connections, where the power-flow is also maximal. Hence, it is quite evident that there are many heterogeneous, rare regions in the EU-HV grid.

V. CONCLUSIONS

Energy security has becoming an extremely important issue these days. The vulnerability of power grids depend very much on the network topology, which has been investigated in our numerical study by comparing the western US and the EU high-voltage grids. The traditional electric swing equations, describing the power-flow among interconnected rotating generators and consumers (machines) is equivalent to a set of second-order Kuramoto

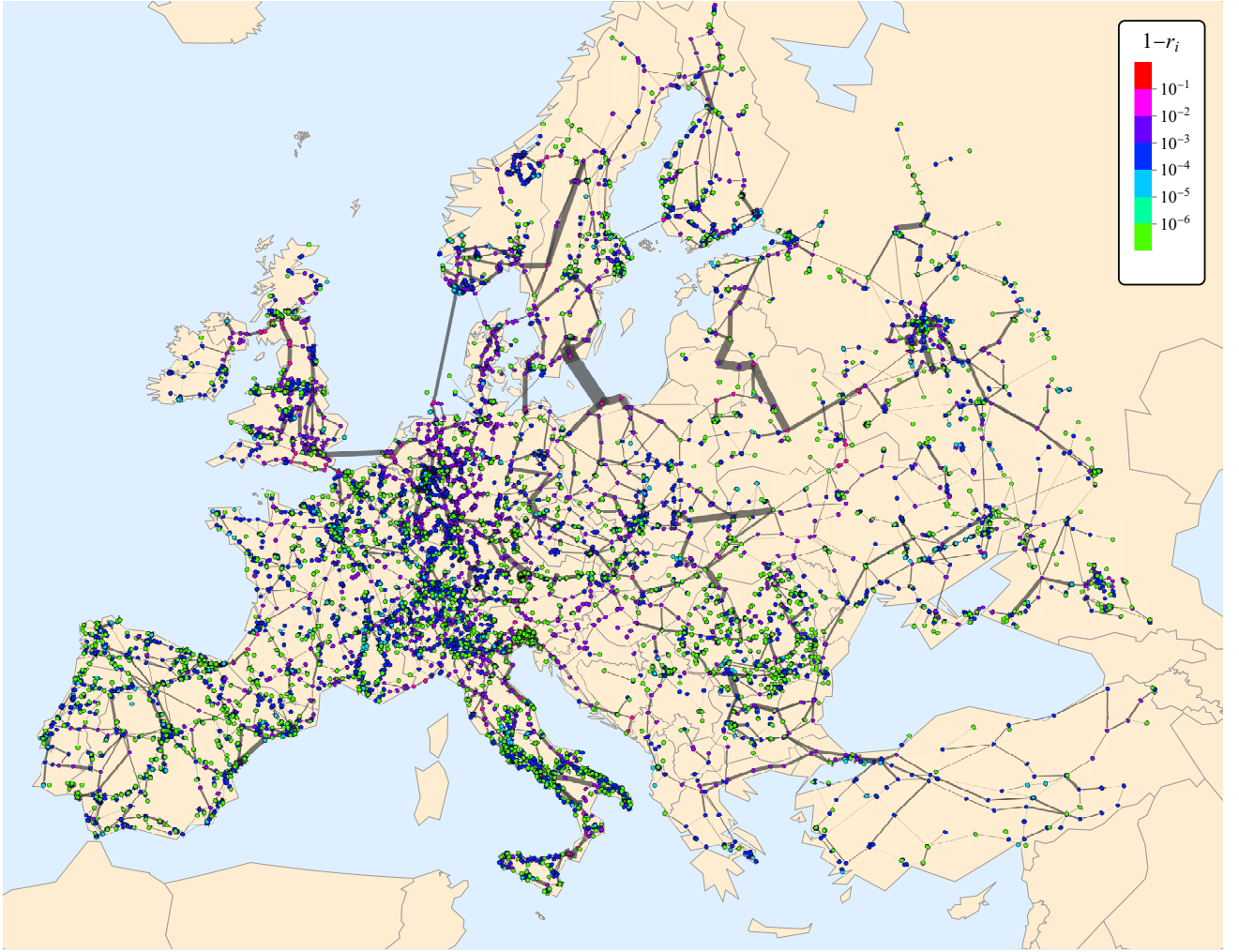


FIG. 17: Local Kuramoto results encoded by the color map as $1 - r_i$. Red corresponds low local synchronization, green to high synchronization. The width of gray edges is proportional to the amplitude of the power flow.

equations, which have been solved numerically on these networks. Our analysis has two parts, a thermalization regime, by which we create stable steady state conditions and a “line-cut” regime, where we allowed dynamical cascade failure events, by removing edges from the graph, whenever the power flows exceed certain threshold values.

The time dependent behavior in the thermalization regime had been followed by analyzing the Kuramoto order parameter of phases as well as by the frequency spread. We used a simplified scenario, in which self-frequencies of the nodes were chosen randomly from a zero centered Gaussian distribution, thus we neglected the power in/out magnitudes of the vertices and their inertia as well as the impedance of the lines. Instead we focused on the effects of dissipation, which can also describe instantaneous feedback.

We compared the frequency spread behavior in the large coupling limit of the solutions with those of the linearized equations and showed that they agree in the

case of coherent initial state using $d = 2, 3$ lattices. This behavior is asymptotically the same as that of the massless Kuramoto equation: $\Omega(t) \sim t^{-d/2}$. However, starting from randomly distributed oscillators we observed faster decays with PL regions after a short initial slip and before finite-size cutoffs. We also found this behavior at the synchronization transitions for the US and EU grids, suggesting that when the linear approximation breaks down due to the fluctuations, coming by large chaoticity at the transition or by initial conditions, non-trivial PL decay can be observed for intermediate times in finite systems.

It is important to note that for the frequency order parameter we expect real phase transitions for $d \geq 2$, which was the case in our networks. For R we expect crossovers in case of $d < 4$, which could be identified by the fluctuation peaks, agreeing with the phase order parameter transition data. However, this crossover point may not coincide with the frequency phase transition point value for the following reason. The crossover point $K_c \rightarrow \infty$ with the system size, while a real phase transition point

should remain a finite value in the thermodynamic limit. In case of US-HV we found a coincidence $K'_c \approx K_c$ regardless of the initial conditions (cf. Fig. 9 and Fig. 19 in the Appendix), while for the EU-HV the phase transition of Ω happens at $K'_c \simeq 44$ as compared to $K_c \simeq 100$ crossover point of the phases (cf. Fig. 13 and Fig. 19 in the Appendix).

The dissipation/feedback factor had mainly delaying effects on the $R(t)$, but increasing α slightly increased $R(t \rightarrow \infty)$ and drastically decreased $\Omega(t \rightarrow \infty)$. In general the Ω order parameter proved to be a more sensitive measure of the synchronization than R .

Following the thermalization we induced failure cascades, by cutting a line from the network. We measured the probability distributions of the line failures, which occurred by the overloads of lines during the power redistribution process, dictated by the second-order Kuramoto dynamics. In the US-HV case, the PDFs of the cascade line cuts were log-normal, for small avalanches in case of high T and K values. For the control parameter regions, where the fluctuations of R showed a peak, the PDFs exhibited PL tails, with continuously changing exponents around $\tau \simeq 1.9$, which agrees with historically observed blackout exponent values. For the EU case we also found the occurrence of steeper PL-s, characterized by $\tau \simeq 3$, in contrast to the US-HV case, but as the observed scaling region is narrow, possibly due to finite sizes, it is hard to distinguish PL-s from log-normal. In any case this is in agreement with the topological analysis result by [5] according to which the marginally fragile EU network might show scale-free cascade distributions as well.

For small T and K parameters non-zero centered PDF “bumps” could be observed, which can be explained by the first-order transition behavior of the second-order Kuramoto model and can be called Dragon Kings following the literature.

In the PL scaling regions we found that the remaining networks after the cascade could exhibit an increase of synchronization. This kind of “islanding” stabilization is also known in the literature as a mean to stabilize power-grids via truncation. The detailed phase transition analysis leads to our most important conclusion for blackout engineering: although “islanding” stabilization does not work for $K > K_c$, it is just the best near the transition point $T_c(K)$, thus self-organization of power systems provides an advantage, as in many other cases, like in neural systems.

Our results suggest that the second-order Kuramoto model exhibits a mixed-order transition in the sense that the steady state order parameter $R(t \rightarrow \infty)$ displays a hysteresis and the frequency order parameter $\Omega(t \rightarrow \infty)$ jumps rapidly at the transition point, with $\Omega(t)$ exhibiting PL tails there. Furthermore, in case of allowing line failures the PDFs of the avalanches also show PL tails. As the consequence of the strong heterogeneity Griffiths phase like frustrated synchronization can also be observed. This is allowed, because the graph dimensions are below $d_c = 4$ and the networks possess modular struc-

ture, which enhances rare region effects.

It is important to note that these PL regions are robust for changes in the networks and the initial perturbations details. The exponents are also invariant for the value of α , but the width of the distribution shrinks, so instantaneous feedback can stabilize or delay cascades, but does not affect the tail behavior of the PDFs.

We have been investigating the heterogeneity in more detail by measuring the local order parameters. As a preliminary result we show how the stronger connected graphical regions are reflected by higher local synchronization.

Appendix

In this Appendix we first show cascade failure distribution results for the EU grid in case of a very low global coupling: $K = 20$ as compared to the transition point: $K_c \simeq 100$. Although the sizes of the avalanches are large, we can't see scale-free behavior up to $T = 0.8$. The graph also shows invariance of PDFs with respect to an initial node or line failure.

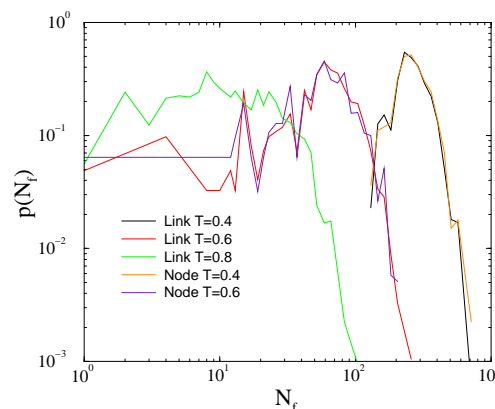


FIG. 18: Probability distribution of line failures for different thresholds for $K = 20$ shown in the legends in case of the EU-HV power grid.

In addition, Fig. 19 shows that there is also a transition in the frequency spread. Since the lower critical dimension for frequency entrainment and phase order parameter are 2 and 4, respectively, in $2 \leq d < 4$, the frequency entrainment transition point K'_c is not necessarily identical with the phase order crossover point K_c [45]. Even though the transition point K'_c for the US-HV case almost coincides with K_c we see that $K'_c \simeq 44$ is rather different from $K_c \simeq 100$ in the EU-HV case.

Acknowledgments

We thank Róbert Juhász and Lilla Barancsuk for the useful comments. Support from the advantaged ELKH

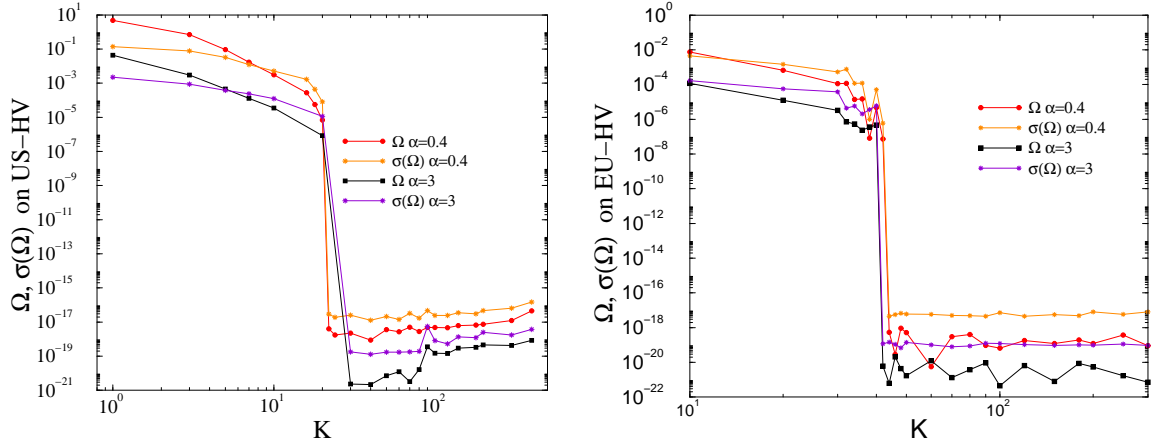


FIG. 19: The stationary frequency spread and the corresponding standard deviation show that the frequency entrainment has a transition point at $K'_c \simeq 20$ for the US-HV grid (Left) and at $K'_c \simeq 20$ for the EU-HV grid (Right). This transition point coincides with K_c for the US-HV case but differs from that of the EU-HV case, as estimated from the peaks of $\sigma(R)$; cf. Figs. 9 and 13.

grant and the Hungarian National Research, Development and Innovation Office NKFIH (K109577) is ac-

knowledgeed. Most of the numerical work was done on KIFU supercomputers of Hungary.

-
- [1] J. A. Acebrón, L. L. Bonilla, C. J. P. Vicente, F. Ritort, and R. Spigler, *Rev. Mod. Phys.* **77**, 137 (2005).
 - [2] A. Arenas, A. Díaz-Guilera, J. Kurths, Y. Moreno, and C. Zhou, *Phys. Rep.* **469**, 93 (2008).
 - [3] G. Ódor and B. Hartmann, *Physical Review E* **98**, 022305 (2018).
 - [4] G. Andersson, P. Donalek, R. Farmer, N. Hatziaargyriou, I. Kamwa, P. Kundur, N. Martins, J. Paserba, P. Pourbeik, J. Sanchez-Gasca, et al., *IEEE Trans. Power Syst.* **20**, 1922 (2005).
 - [5] M. R. Casals, Ph.D. thesis, UPC Barcelona (2009).
 - [6] M. Rosas Casals and B. Corominas Murtra, *WIT Trans. Ecol. Environ.* **121**, 527 (2009).
 - [7] A. Abedi, L. Gaudard, and F. Romerio, *Reliab. Eng. Syst. Saf.* **183**, 153 (2019).
 - [8] P. Bak, C. Tang, and K. Wiesenfeld, *Phys. Rev. Lett.* **59**, 381 (1987).
 - [9] B. A. Carreras, D. E. Newman, I. Dobson, and A. B. Poole, *IEEE Trans. Circuits Syst. I: Regul. Pap.* **51**, 1733 (2004).
 - [10] I. Dobson, B. A. Carreras, V. E. Lynch, and D. E. Newman, *Chaos* **17**, 026103 (2007).
 - [11] G. Filatrella, A. H. Nielsen, and N. F. Pedersen, *Eur. Phys. J. B* **61**, 485 (2008).
 - [12] R. Carareto, M. S. Baptista, and C. Grebogi, *Commun. Nonlinear Sci. Numer. Simul.* **18**, 1035 (2013).
 - [13] Y.-P. Choi, S.-Y. Ha, and S.-B. Yun, *Physica D* **240**, 32 (2011).
 - [14] Y.-P. Choi, Z. Li, S.-Y. Ha, X. Xue, and S.-B. Yun, *J. Differ. Equ.* **257**, 2591 (2014).
 - [15] F. Dörfler and F. Bullo, *SIAM J. Control Optim.* **50**, 1616 (2012).
 - [16] F. Dörfler and F. Bullo, *Automatica* **50**, 1539 (2014).
 - [17] M. Frasca, L. Fortuna, A. S. Fiore, and V. Latora, in *Proceedings of the PHYSCON 2011, Leon, Spain* (2011).
 - [18] S. Olmi, A. Navas, S. Boccaletti, and A. Torcini, *Phys. Rev. E* **90**, 042905 (2014).
 - [19] R. S. Pinto and A. Saa, *Physica A* **463**, 77 (2016).
 - [20] K. Schmietendorf, J. Peinke, R. Friedrich, and O. Kamps, *Eur. Phys. J.: Spec. Top.* **223**, 2577 (2014).
 - [21] J. Grzybowski, E. Macau, and T. Yoneyama, *Chaos* **26**, 113113 (2016).
 - [22] H. Taher, S. Olmi, and E. Schöll, *Phys. Rev. E* **100**, 062306 (2019).
 - [23] F. Hellmann, P. Schultz, P. Jaros, R. Levchenko, T. Kapitaniak, J. Kurths, and Y. Maistrenko, *Nature Comm.* **11**, 1 (2020).
 - [24] Y. Kuramoto, *Chemical Oscillations, Waves, and Turbulence*, Springer Series in Synergetics (Springer Berlin Heidelberg, 2012), ISBN 9783642696893.
 - [25] H. Hong, H. Chaté, H. Park, and L.-H. Tang, *Phys. Rev. Lett.* **99**, 184101 (2007).
 - [26] T. Vojta, *J. Phys. A* **39**, R143 (2006).
 - [27] R. B. Griffiths, *Phys. Rev. Lett.* **23**, 17 (1969), ISSN 0031-9007.
 - [28] G. Ódor, *Physical Review E* **89**, 042102 (2014).
 - [29] S. Biswas and L. Goehring, *Europhys. Lett.* **126**, 44002 (2019).
 - [30] P. Villegas, P. Moretti, and M. A. Munoz, *Sci. Rep.* **4**, 1 (2014).
 - [31] P. Villegas, J. Hidalgo, P. Moretti, and M. A. Muñoz, in *Proceedings of ECCS 2014* (Springer, 2016), pp. 69–80.
 - [32] A. P. Millán, J. J. Torres, and G. Bianconi, *Sci. Rep.* **8**, 1 (2018).
 - [33] G. Ódor and J. Kelling, *Sci. Rep.* **9**, 1 (2019).
 - [34] G. Ódor, J. Kelling, and G. Deco, *J. Neurocomputing* **461**, 696 (2021).
 - [35] G. Ódor, G. Deco, and J. Kelling, *Phys. Rev. Research*

- 4, 023057 (2022).
- [36] G. Ódor and B. Hartmann, *Entropy* **22**, 666 (2020).
 - [37] B. Schäfer, D. Witthaut, M. Timme, and V. Latora, *Nat. Commun.* **9**, 1 (2018).
 - [38] F. Kaiser, V. Latora, and D. Witthaut, *Nat. Commun.* **12**, 1 (2021).
 - [39] F. Kaiser and D. Witthaut, *Phys. Rev. Res.* **3**, 023161 (2021).
 - [40] R. Baldick, B. Chowdhury, I. Dobson, Z. Dong, B. Gou, D. Hawkins, H. Huang, M. Joung, D. Kirschen, F. Li, et al., in *2008 IEEE Power and Energy Society General Meeting-Conversion and Delivery of Electrical Energy in the 21st Century* (IEEE, 2008), pp. 1–8.
 - [41] A. Esmaeilian and M. Kezunovic, *IEEE Trans. Ind. Appl.* **53**, 622 (2016).
 - [42] D. Sornette and G. Ouillon, *Eur. Phys. J.: Spec. Top.* **205**, 1 (2012).
 - [43] S. di Santo, R. Burioni, A. Vezzani, and M. A. Munoz, *Phys. Rev. Lett.* **116**, 240601 (2016).
 - [44] G. Mikaberidze and R. M. D’Souza, *Chaos* **32**, 053121 (2022).
 - [45] H. Hong, H. Park, and M. Choi, *Phys. Rev. E* **72**, 036217 (2005).
 - [46] J. Grainger, J. and D. Stevenson, W., *Power system analysis* (McGraw-Hill, 1994), ISBN ISBN 978-0-07-061293-8.
 - [47] K. Ahnert and M. Mulansky, *Boost::odeint*, URL <https://odeint.com>.
 - [48] D. Demidov, *Vexcl c++ vector expression template library for opencl/cuda/openmp*, URL <https://vexcl.readthedocs.io>.
 - [49] K. Jeffrey, S. Deng, L. Barancsuk, B. Hartmann, and G. Ódor (to be published).
 - [50] M. Newman, *Networks: An Introduction* (Oxford University Press, 2010).
 - [51] *Gephi tool*, <https://gephi.org>, URL <https://gephi.org>.
 - [52] *Us power grid*, <http://konect.cc/networks/>, URL <http://konect.cc/networks/>.
 - [53] *Eu-hv power grid*, <https://www.power.scigrid.de/pages/downloads>, URL <https://www.power.scigrid.de/pages/downloads.html>.
 - [54] M. Rosas-Casals and R. Solé, *International Journal of Electrical Power & Energy Systems* **33**, 805 (2011).
 - [55] B. Hartmann and V. Sugár, *Sci. Rep.* **11**, 1 (2021).
 - [56] D. J. Watts and S. H. Strogatz, *Nature* **393**, 440 (1998).
 - [57] A. Fronczak, P. Fronczak, and J. A. Holyst, *Phys. Rev. E* **70**, 056110 (2004).
 - [58] M. D. Humphries and K. Gurney, *PloS One* **3**, e0002051 (2008).
 - [59] G. Ódor and B. de Simoni, *Phys. Rev. Res.* **3**, 013106 (2021).
 - [60] J. G. Restrepo, E. Ott, and B. R. Hunt, *Phys. Rev. E* **71**, 036151 (2005).
 - [61] M. Schröder, M. Timme, and D. Witthaut, *Chaos* **27**, 073119 (2017).